Corrosion Science 127 (2017) 157–167

Contents lists available at ScienceDirect

Corrosion Science

journal homepage: www.elsevier.com/locate/corsci

A research on the corrosion and stress corrosion cracking susceptibility of 316L stainless steel exposed to supercritical water

Xianglong Guo[a], Kai Chen[a], Wenhua Gao[a], Zhao Shen[b], Ping Lai[a], Lefu Zhang[a,*]

[a] School of Nuclear Science and Engineering, Shanghai JiaoTong University, NO. 800 Dongchuan Road, Shanghai, China
[b] Department of Materials Science, University of oxford,Parks Road, Oxford OX1 3PH, UK

ARTICLE INFO

Keywords:
316L stainless steel
Supercritical water
Microstructure characterization
Corrosion
Stress corrosion cracking

ABSTRACT

This study investigated the corrosion and stress corrosion cracking susceptibility of 316L stainless steel exposed to 550 °C and 600 °C supercritical water. XRD, SEM, EDS and EBSD analyses have been carried out to characterize the microstructure of the tested specimens. Results indicate that increasing the test temperature reduced the corrosion and SCC resistance of 316L SS. The oxide scale of corroded specimen shows a duplex structure, and the fracture analysis indicates that the formation of Fe_3O_4 'channels' in the Fe-Cr spinel layer contributes to the intergranular and transgranular SCC of the materials in 550 °C and 600 °C SCW.

1. Introduction

Generation IV reactors are attractive due to their high efficiency and safety [1,2]. The supercritical water cooled reactor (SCWR) is one of the most promising of the six innovative Generation IV reactor concepts because it offers advantages, such as simplification of components and higher efficiency [3,4]. By operating above the thermodynamic critical point of water (374 °C, 22.1 MPa), a single phase coolant is used in SCWR and many components, such as steam generators, steam separators, dryers, recirculation and jet pumps are not necessary [5,6]. Thus, the design of the reactor is greatly simplified.

In SCWR, the fuel cladding experiences the most severe conditions among the in-core structural components. During normal operation, the temperature on the fuel cladding can be 600 °C, and it can be even higher during transients. The higher the operating temperature, the higher the possibility that the fuel cladding material will fail due to creep [7], corrosion [6,8] or stress corrosion cracking (SCC) [6], which can result in leakage of fission products and pose great challenges to the reactor safety.

Stainless steels (SS) [8,9], nickel based alloys [10,11] and oxide dispersion strengthened steels (ODS) [12,13] have been proposed as candidate materials for fuel cladding and other core components in SCWRs, and extensive research has been conducted to examine the corrosion and SCC performance of those materials [14–17]. Among the candidate materials, austenitic stainless steels (SSs) are the least expensive, and some research [6] indicates that their corrosion resistance are better than nickel-based alloys. However, other research [18,19] reported that the corrosion rate of 316L SS was much higher than nickel-based alloys.

Maderuelo [20] reported that 316L SS was susceptible to SCC when exposed to supercritical water, and the susceptibility increased with increasing temperature. Teysseyre and Was [21] compared the SCC behavior of 304L SS, 316L SS, Alloy 625 and Alloy 690, and found that all alloys displayed some intergranular stress corrosion cracking (IGSCC) at 400 °C and 550 °C. Shen and Zhang [22] studied the effect of temperature on the SCC behavior of 316Ti SS in SCW, and concluded that the failure mode of 316Ti SS was IGSCC at 550 °C, while no SCC was observed at temperatures of 600 °C and 650 °C. To date, the results on the corrosion and SCC behavior of SSs in SCW are limited and controversial, so further research is needed.

The present work studies the corrosion and SCC susceptibility of 316L SS exposed to 550 °C and 600 °CSCW. The microstructure and composition of oxide scale formed on the 316L SS is examined. Special emphasis is placed on the analysis of the fracture process of the materials and the SCC mechanism.

2. Experimental procedure

Type 316L SS has been widely used in Generation II and III light water reactors and thus it was evaluated in this program. The type 316L SS was tested in the solution annealed condition. The chemical composition and microstructure of this material are shown in Table 1 and Fig. 1, respectively.

The microstructure is typical of austenitic SS and the average grain size is about 30 μm.

Specimens for corrosion and slow strain rate tension (SSRT) testing were cut from the solution annealed plate and the surfaces were

* Corresponding author.
E-mail address: lfzhang@sjtu.edu.cn (L. Zhang).

http://dx.doi.org/10.1016/j.corsci.2017.08.027
Received 9 December 2016; Received in revised form 21 August 2017; Accepted 23 August 2017
Available online 26 August 2017
0010-938X/ © 2017 Elsevier Ltd. All rights reserved.

Table 1
Chemical composition of 316L SS(wt.%).

Steel	Fe	Cr	Ni	Mo	Mn	Si	Cu	V	P	S	Co	C
316L SS	Bal.	16.38	9.60	3.15	1.60	0.41	0.51	0.07	0.03	0.01	0.28	0.01

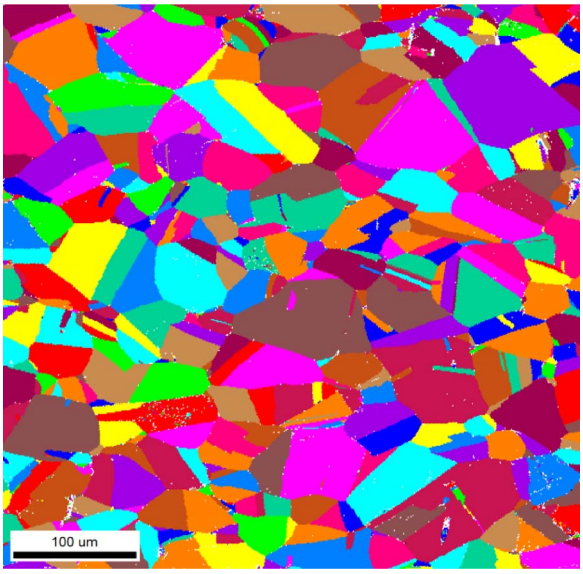

Fig. 1. EBSD image of the solution annealed 316L SS.

mechanically abraded with sandpaper to 4000# grit. The samples were then polished with diamond Al_2O_3 to a final surface roughness of 0.4 μm. The dimensions of the samples for the corrosion test was 20 × 10 × 2 mm, and the gauge section of the SSRT specimens was 2 × 3 mm with a gauge length of 15 mm.

The corrosion and SSRT tests were conducted in an autoclave connected to a water chemistry control loop. Fig. 2 shows the schematic representation of the test system, which can operate up to 30 MPa and 670 °C. The testing conditions for the corrosion and SSRT tests are listed in Table 2.

The oxygen content was controlled by bubbling high-purity argon into the water. For the corrosion test, the exposure periods were 100, 300, 600, 1000 and 1500 h after each exposure period, the dimensions and weight of the corroded samples were measured and the weight gain per unit area was calculated. Scanning electron microscope (SEM), energy dispersive spectroscopy (EDS), electron back-scattered diffraction (EBSD) and X-ray diffraction analysis (XRD) techniques were used to characterize the microstructure and phase evolution in the corrosion and SSRT tests.

Table 2
Test conditions for the corrosion and SSRT tests.

Tests	General corrosion	SSRT	
Parameters		Water	Argon
Temperature	550 °C 600 °C	550 °C 600 °C	550 °C 600 °C
Inlet conductivity	≤0.1 μS/cm	≤0.1 μS/cm	/
Pressure	25 MPa	25 MPa	0.1 MPa
Oxygen concentration (in mass)	≤5 ppb	≤5 ppb	/
Strain rate (s^{-1})	/	1×10^{-6}	1×10^{-6}
pH (room temperature)	7	7	/

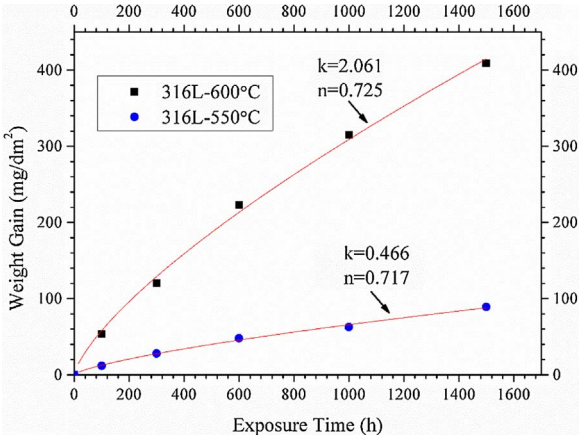

Fig. 3. Weight gain vs. time of 316L SS in 550 °C and 600 °C SCW.

3. Results and discussion

3.1. Weight gain and oxide scale analysis

Fig. 3 shows the mass gain of the samples after being immersed in SCW

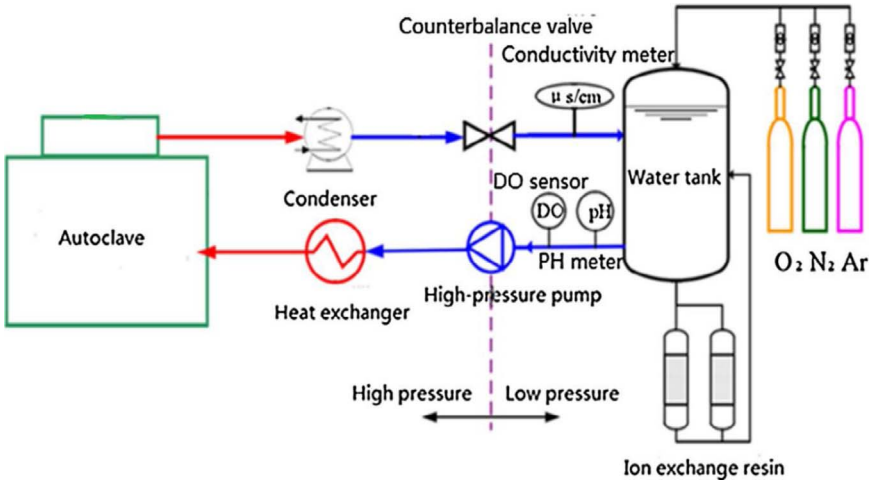

Fig. 2. Schematic of the corrosion and SSRT test system.

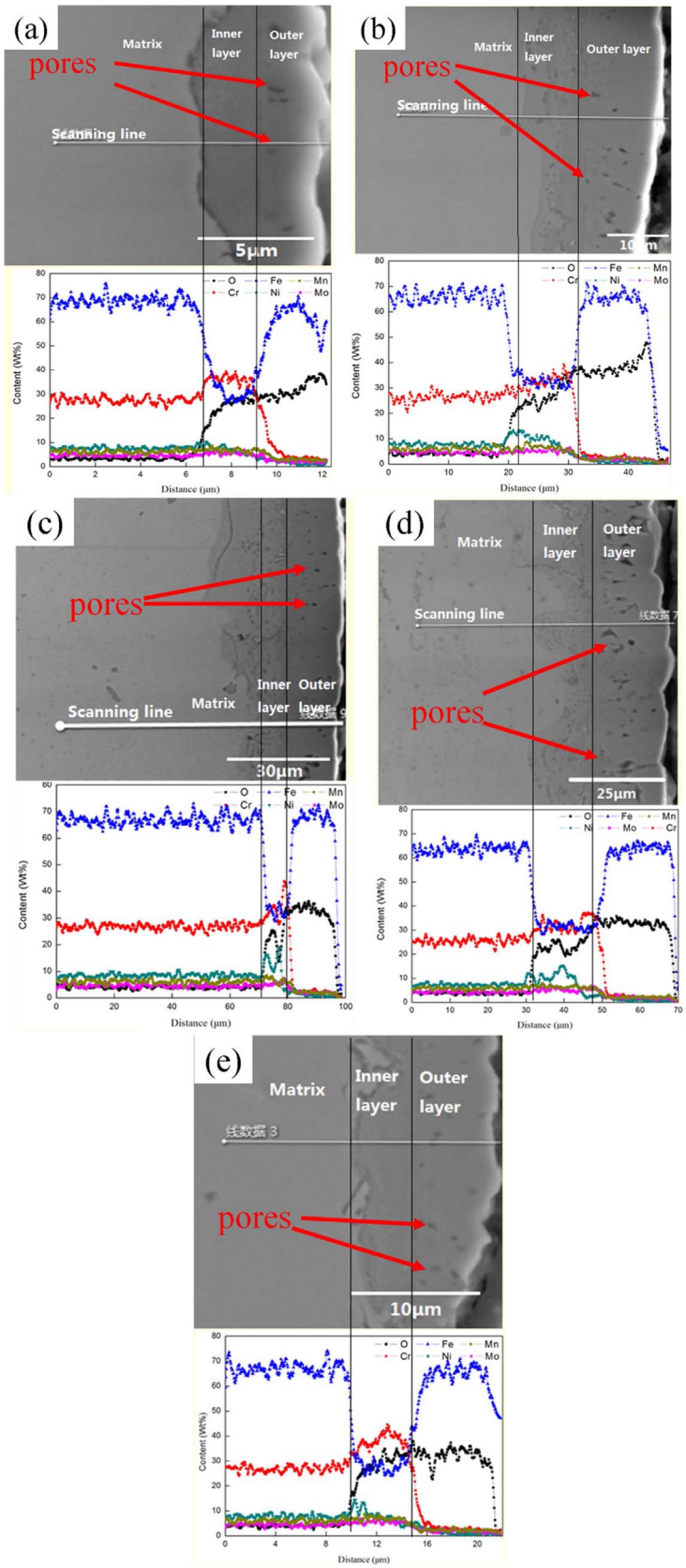

Fig. 4. SEM image and EDS analysis results from a cross section of the specimen tested at (a) 600 °C/100 h, (b) 600 °C/600 h, (c) 600 °C/1000 h, (d) 600 °C/1500 h and (e) 550 °C/1500 h.

for different times. At all temperatures, as testing time increased, the weight gain of the samples increased. The rate of weight gain decreased with testing time, more slowly at 600 °C than 550 °C. The weight gain of samples tested at 600 °C is much higher than at 550 °C.

Prior research [6,23,24] also reported that the weight gain of 316L SS and other materials increased with temperature in SCW or subcritical water. In the present research, the weight gain (Δw) of 316L SS as a function of exposure time can be fitted by the following equation:

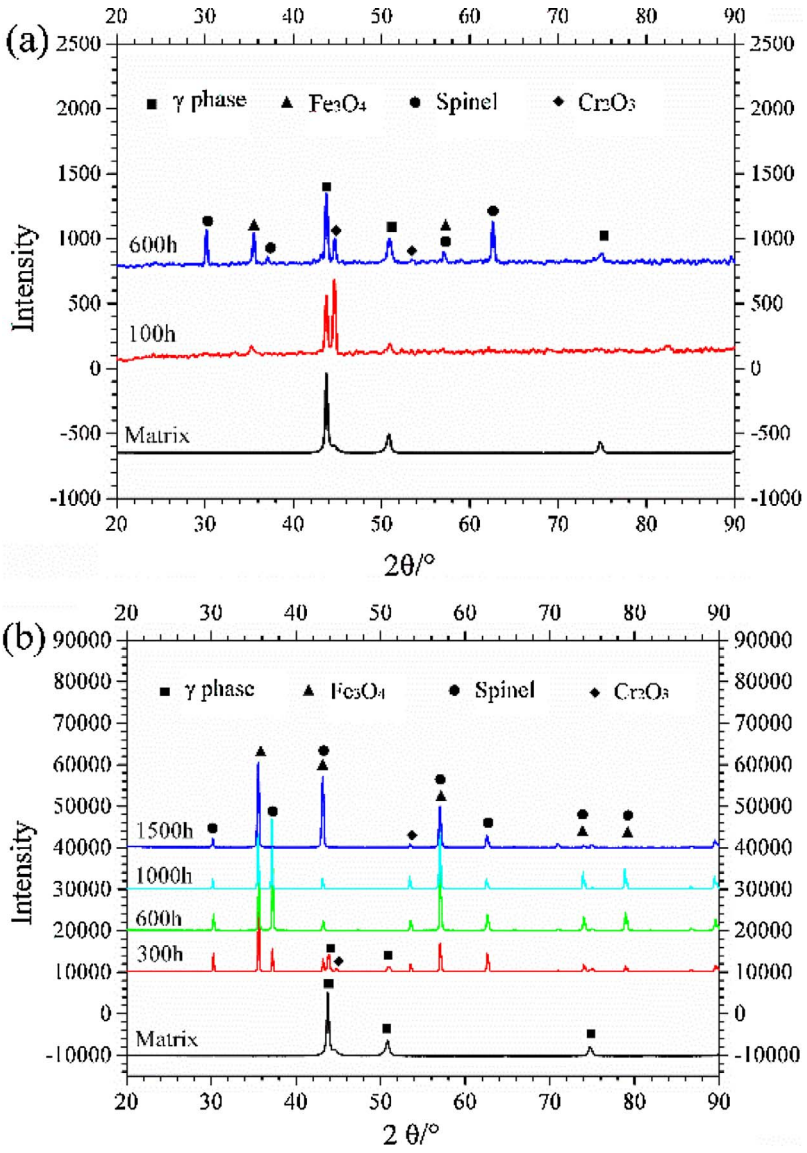

Fig. 5. XRD patterns of 316L SS exposed to (a) 550 °C and (b) 600 °C SCW for different times.

$$\Delta w = kt^n \quad (1)$$

where t is the exposure time, n is a parameter reflecting the time dependence of the oxide growth, and k is the rate constant.

The fitted results are also shown in Fig. 3. k increases with temperature, reflecting a higher weight gain at 600 °C than at 550 °C. The time exponent (n) for samples tested at 550 °C and 600 °C is 0.717 and 0.725, respectively. The response apparently follows a law between parabolic and linear, indicating a relatively low protectiveness of the oxide. For parabolic growth, diffusion of metal cations and oxygen anions is the rate-controlling step. For stainless steels exposed to SCW, deviation from the parabolic law has been reported [25,26] and this may be attributed to the microstructure of the oxide formed on the surface of the specimens, as discussed later.

To examine the corrosion behavior of 316L SS in SCW, the cross section of the samples tested at 550 °C and 600 °C is examined with SEM and EDS (Fig. 4). The oxide scale contains two layers: the outer one and the inner one, regardless of the test temperature. The EDS results indicate that the outer layer is rich in Fe and O, and depleted of Cr and Ni, as well as other elements. The inner layer is rich in Cr, and the Fe content in the inner layer is greatly reduced compared with the outer layer and the matrix, indicating that a Cr-enriched oxide is formed. Pores are observed in outer layer of the oxide scale, even for the specimen exposed to 600 °C SCW for only 100 h. The formation of pores leads to faster growth of inner layer by access of SCW through those pores, and this could be an explanation for why the oxide formation on 316L SS does not follow a parabolic law.

XRD analysis was conducted to identify the phases in the oxide (Fig. 5). At 550 °C(Fig. 5(a)), Cr_2O_3 and Fe_3O_4 are detected on the sample exposed for 100 h. Fe-Cr spinel is also detected, but its amount is limited compared to Cr_2O_3 and Fe_3O_4. When the exposure time is increased to 600 h, the content of Fe-Cr spinel in the oxide scale increases greatly, while the content of Cr_2O_3 decreases. This is because with increasing exposure time, Cr_2O_3 can react with Fe to form Fe-Cr spinel, which decreases the content of Cr_2O_3 in the oxide scale. The other reason is that the thickness of the oxide scale increases with the increasing exposure time, which can inhibit XRD signal from Cr_2O_3 in the inner oxide.

At 600 °C(Fig. 5(b)), the phase of the oxide at 300 h, 600 h, 1000 h and 1500 h is the same, and Cr_2O_3, Fe_3O_4 and Fe-Cr spinel are detected. When the exposure time increases to 1500 h, the amount of Cr_2O_3 is greatly reduced, for the same reason as in the 550 °C samples.

Thus, it is reasonable to conclude that the phase in the outer oxide layer is Fe_3O_4, while in the inner layer, the main phase is $FeCr_2O_4$. No Fe_2O_3 was detected in the oxide film, even at test temperatures as high as 600 °C, which contradicts some previous studies [27,28] that Fe_2O_3 is detected on

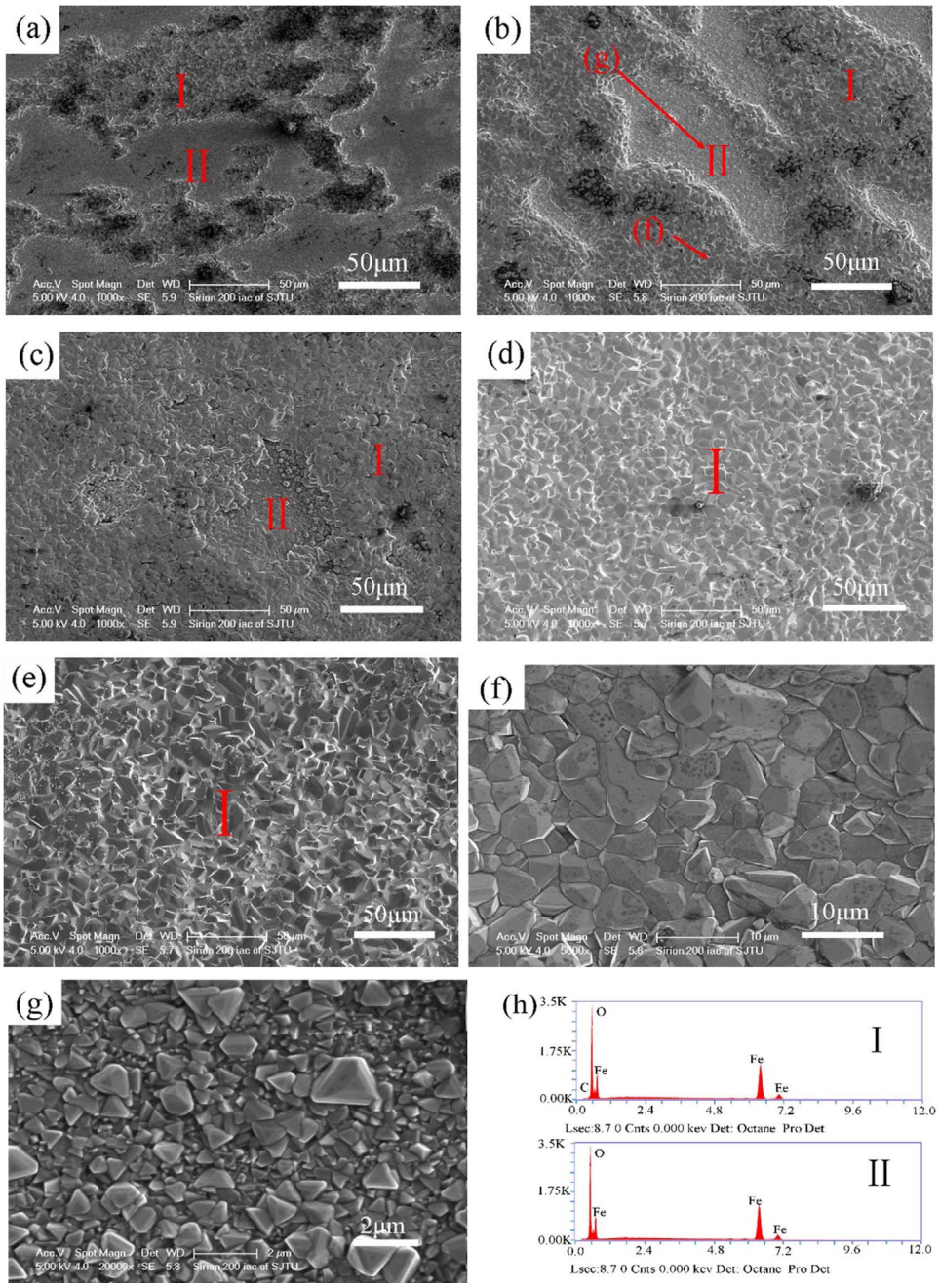

Fig. 6. SEM images of the surface of specimens exposed to SCW (600 °C/25 MPa) for (a) 100 h, (b) 300 h, (c) 600 h, (d) 1000 h, (e) 1500 h and (f) magnified image of region I in (b), (g) magnified image of region II in (b), (h) EDS results for region I and II.

the outmost layer of the oxide scale. The phases formed on the surface of 316L SS exposed to SCW depends on: (1) the content of oxygen in the SCW; (2) the test temperature and (3) the composition of the alloy. In the present research, the oxygen content in the water is very low because Ar is continuously bubbled into the water, so the oxygen partial pressure on the outer surface of the oxide scale exposed to SCW is very low [29,30].

Fig. 6 shows the evolution of the surface morphology with increasing exposure time. When the test time is ≤600 h, the surface of the corroded samples consists two different morphologies, as indicated by I and II in Figs. 6(a) to (c). The area of part II decreases with time and Fig. 6(d) and (e) show that the surface morphology is uniform and only contains the morphology I in Fig. 6(a) to (c).

Magnified images of part I and II are shown in Fig. 6 (f) and (g), respectively. The grain size of part I is much larger than part II. EDS examination reveals that the compositions of part I and II are the same, and only Fe and O are detected. The outmost oxide layer is Fe_3O_4, which is not formed uniformly on the surface.

Fig. 7 is a cross-sectional SEM micrograph with corresponding EDS elemental maps of 316L SS exposed to SCW for 1500 h at 550 °C (Fig. 7(a)) and 600 °C (Fig. 7(b)). It can be found that the thickness of the oxide scale at 600 °C is much greater than at 550 °C, in agreement with the weight gain tests. The compositions of the oxide scales formed at the two temperatures is similar. The oxide scale formed in 550 °C SCW contains two layers: an outer one rich in Fe and O, but depleted of other elements, and an inner one composed of Fe, Cr and O. Ni enrichment near the interface of the matrix and the inner layer is observed on samples exposed in 550 °C and 600 °C SCW. Of the main constituents of 316SS, Ni is the noblest element in SCW environment, and it can diffuse away from areas undergoing oxidation. This observation indicates that, although the corrosion rate of the materials tested at different temperature is different, the composition of the oxide scale is the same.

Thus, the oxidation process of 316L SS in SCW is schematically shown in Fig. 8. Early in the oxidation process in SCW, protective

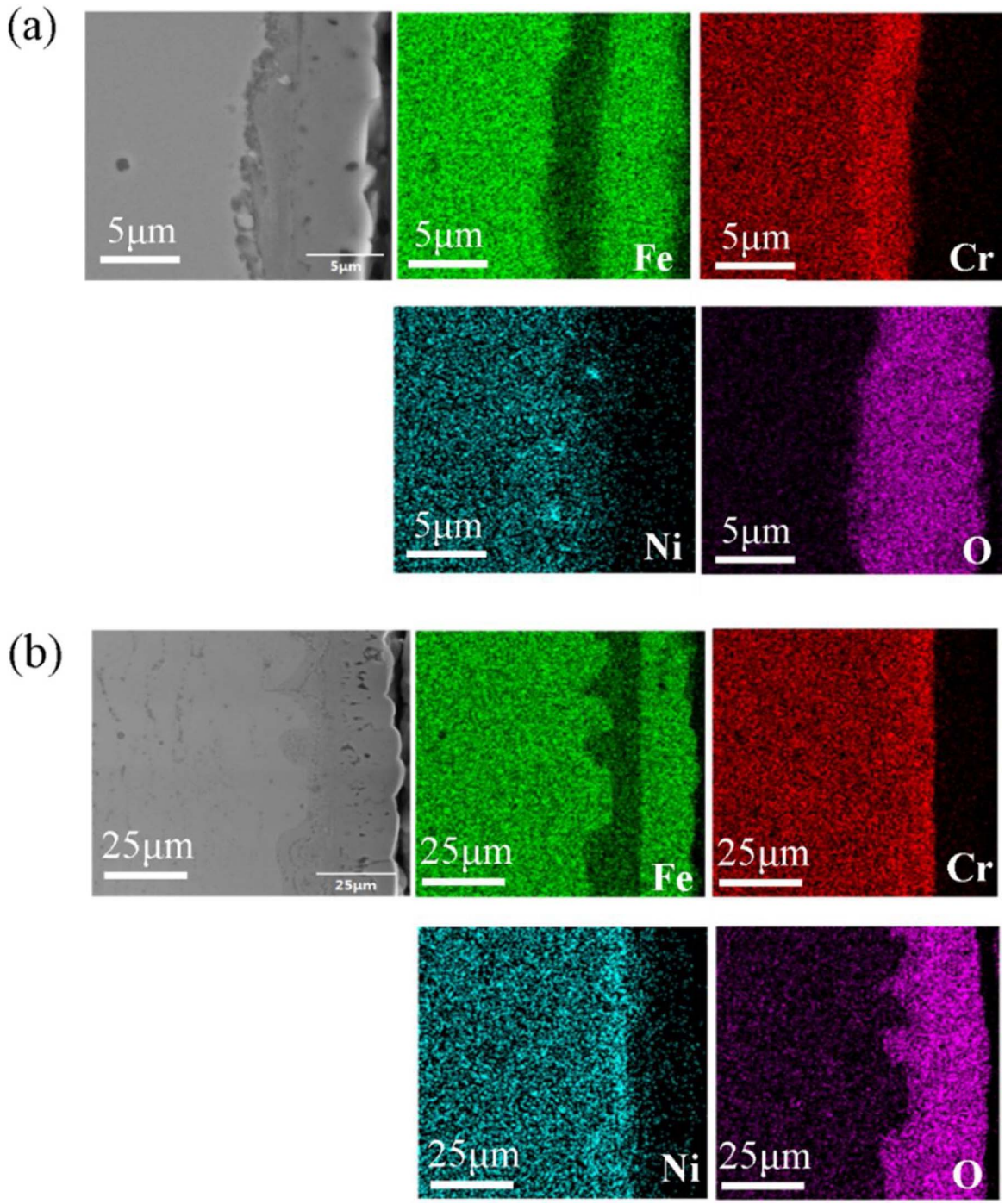

Fig. 7. Cross-sectional SEM micrograph with corresponding EDS elemental maps of Fe, Cr, Ni and O of 316L SS exposed to (a) 550 °C and (b) 600 °C SCW for 1500 h.

chromium oxide can be formed, given the high oxygen affinity of Cr, and this has been confirmed by the XRD analysis shown in Fig. 5. Cr_2O_3 is formed through the following reaction:

$$2Cr + 3H_2O = Cr_2O_3 + 3H_2 \quad (2)$$

The cross sectional EDS line analysis (Fig. 4) shows that there is no area that contains only Cr and O, which indicates that no continuous Cr_2O_3 film is formed. Thus Cr_2O_3 forms only as discrete islands in the matrix, as schematically shown in Fig. 8(b). No continuous film of Cr_2O_3 forms because: (1) the low oxygen content in the SCW, and (2) the relative low Cr content in 316L SS (16.38% Cr). It has been reported that when the Cr content in the steel is higher than ~20 wt% [31], a more protective and continuous Cr_2O_3 film can be formed. The absence of continuous Cr_2O_3 also contributes to fast diffusion of Fe cations to the outer oxide, so sufficient Fe cations are supplied for the growth of Fe_3O_4 oxide and stops the Fe_3O_4 from being further oxidized to Fe_2O_3.

The formation of Cr_2O_3 leads to Cr depletion in the metal matrix, so Fe can react with the water to form Fe_3O_4 (Fig. 8c) according to the following reaction:

$$3Fe + 4H_2O = Fe_3O_4 + 4H_2 \quad (3)$$

Cr_2O_3 can react with Fe to form Fe-Cr spinel according to the following equation:

$$Cr_2O_3 + H_2O + Fe = FeCr_2O_4 + H_2 \quad (4)$$

so the Fe-Cr spinel layer is formed.

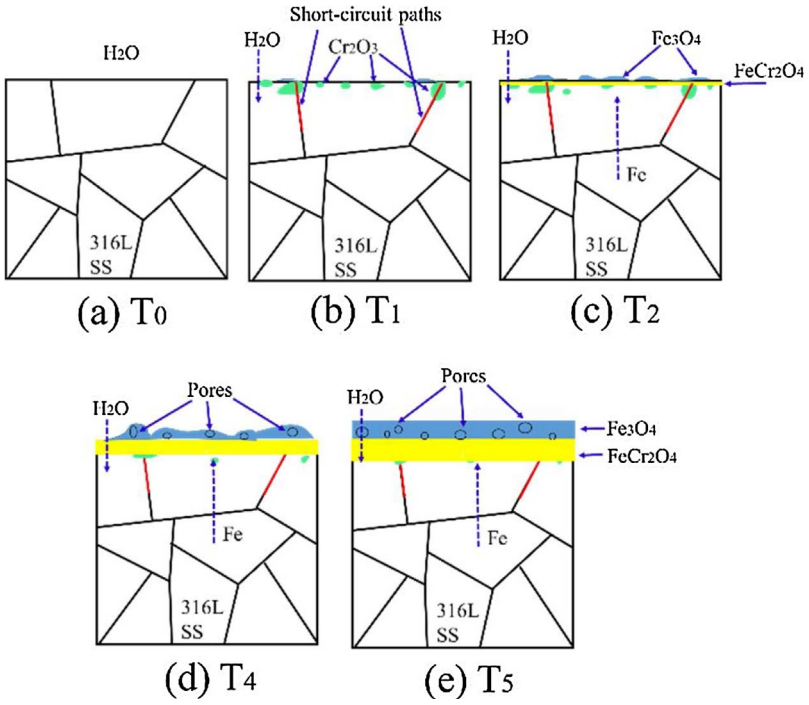

Fig. 8. Schematic of the oxidation process for 316L SS in SCW.

Fe can diffuse through both the matrix grain interior and boundaries to the surface, however, the diffusibility of Fe through the grain boundary is much higher than that through the grain interior [32,33], so in the oxidation process, Fe first diffuses to the oxide-metal interface along the short-circuits such as grain boundaries to react with oxygen. Fe diffusion in a Fe-Cr spinel layer is about 3 times faster than Cr, so Fe can diffuse through the Fe-Cr spinel and react with H_2O to form Fe_3O_4 in the oxidation process. The grains of the Fe_3O_4 on the top of the short-circuit paths will grow faster, producing a larger grain size. This explains the evolution of the morphology of the oxide surface with time, as shown in Fig. 6. At the outer layer/SCW interface, Fe^{2+} can also react with oxygen to form iron oxide. However, in these experiments, argon was continuously bubbled into the SCW and the oxygen content in the SCW is $\leq$5ppb.

Observation of the cross section of the oxide scale (Fig. 4) indicates that pores are formed in the Fe_3O_4 film, even in areas near the Fe-Cr spinel and the interface between the Fe-Cr spinel and Fe_3O_4 film. Tan [34] reported that the formation of pores in the Fe_3O_4 film is closely correlated with the diffusion mechanism of Fe ion in Fe_3O_4, and the pores are formed as the vacancy diffusion mode dominates. Some researchers [35,36] pointed out that the release of H_2 in the oxidation process can be trapped or ejected in the Fe_3O_4 layer, causing pores to form. Also, $Fe(OH)_2^{(g)}$ is thought to be volatile [35] and could be involved in the metal wastage process when the Fe based alloys are exposed to high temperature water. $Fe(OH)_2^{(g)}$ may be formed in the following reactions:

$$Fe_3O_4 + 3H_2O = 3Fe(OH)_2^{(g)} + 1/2O_2 \quad (5)$$

As a result, the possible vaporization of $Fe(OH)_2^{(g)}$ could also lead to the formation of pores in the outer oxide (Fe_3O_4) layer. In the present research, the release of the hydrogen and the dissolution of the oxide are to some extent responsible for the formation of pores in the oxide scale. However, a full understanding of the pore formation mechanism in the Fe_3O_4 layer still needs further investigation.

3.2. Stress-strain curves and SCC mechanism

Fig. 9(a) and (b) show the stress-strain curves of 316L SS tested in argon and SCW, respectively. The mechanical properties of the materials, the yield strength, ultimate strength and the fracture strain of the materials are summarized and listed in Table 3.

At higher temperature, the fracture strain is greatly reduced, both in argon and SCW. Compared with the materials tested at 550 °C, the fracture strain of the 316L SS tested in 600 °C argon and SCW is reduced by 25.6%and 49.8%, respectively. However, test temperature has less effect on the yield strength. When 316L SS is tested in 550 °C water, the yield strength is 13.6% higher than when tested in 600 °C SCW. The yield strength of 316L SS tested in 550 °C and 600 °C argon is almost the same.

In tensile tests of face centered cubic materials, the deformation mode can shift from planar slip to cross slip with increased deformation [37,38], which results in the formation of dislocation tangles. The saturation of dislocation tangles reduces the strain hardening capacity of the materials. Mechanical twinning and martensitic transformation can also be activated in the deformation process of SSs because of their low stalking fault energy [39], and compared with dislocation tangles, they provide a more sustainable hardening mechanism. So if mechanical twinning and martensitic transformation are activated during plastic deformation, the hardening capacity of the materials can be sustained. In the present research, As the test temperature is increased, the stalking fault energy of the materials is increasing, which results in more cross slip in the early stage of the plastic deformation, so the strain hardening capability of the materials is reduced. With the increasing test temperature, the mobility of dislocations is enhanced, causing more dislocation interaction and a higher rate of thermal dislocation annihilation. So in the present research, the yield, ultimate strength and fracture strain of 316L SS are decreasing as the test temperature increases, both in argon and SCW.

Comparison of the mechanical properties of 316L SS tested at the same temperature indicates tests in water show lower fracture stress and strain than tests in argon, as shown in Table 3, which reflects of the contribution of SCC. Prior research [17,22,40] indicates that the SCC susceptibility of type 316 SS is very sensitive to test temperature, and up to 500 °C, the SCC susceptibility increases with test temperature. However, when the test temperature is above than 500 °C, the SCC susceptibility of the SSs is greatly reduced due to the softening of the materials at higher temperature. Tsuchya [41] even reported that no SCC (determined by%IG) was observed on the fracture surface of 304

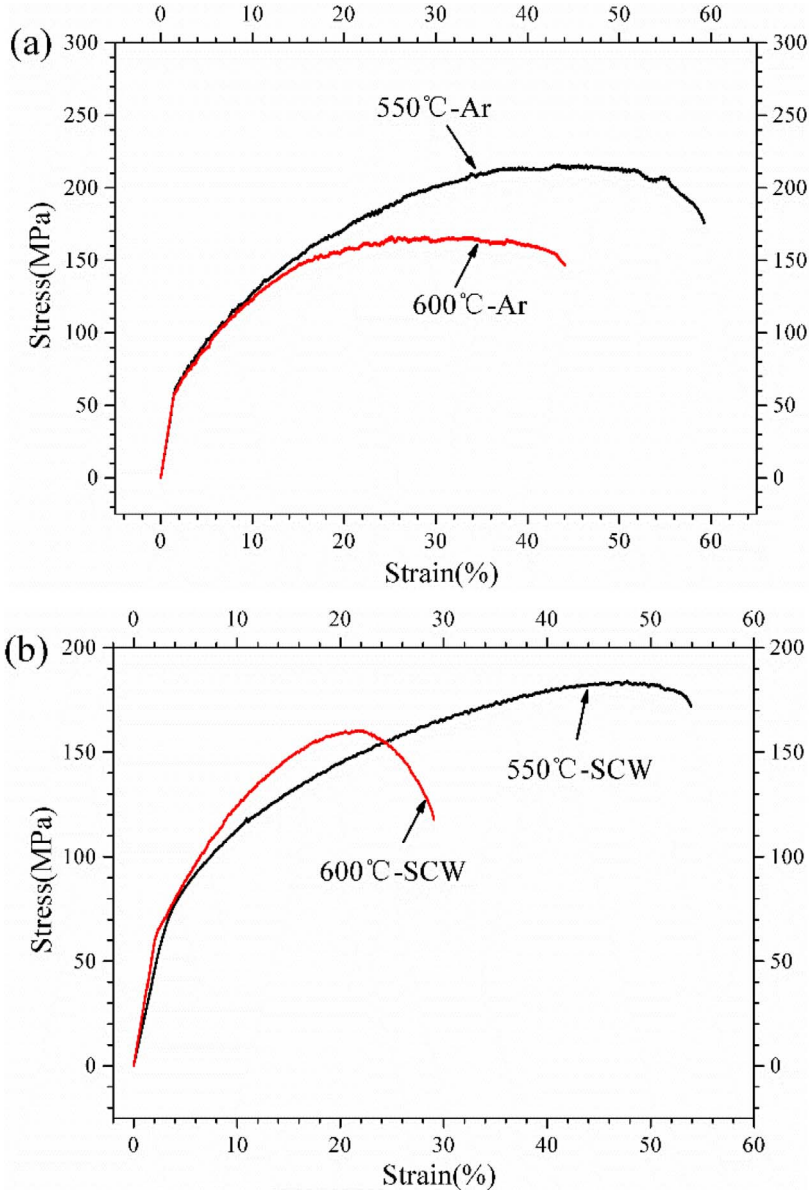

Fig. 9. Stress-strain curves of 316L SS tested in (a) argon and (b) SCW at 550 °C and 600 °C.

Table 3
Summary of the mechanical properties of 316L SS tested in SCW and argon.

Mechanical properties	SCW		Argon	
	550 °C	600 °C	550 °C	600 °C
Yield strength σ_y (MPa)	72.65	62.77	58.67	57.94
Ultimate strength σ_u (MPa)	183.93	160.52	215.95	166.57
Fracture strain ε (%)	53.91	29.04	59.26	44.06

and 316 SS when the specimens are tested in 550 °C SCW. In the present research, the fracture surface and the gauge section near the fracture surface of the samples tested in SCW are examined and the results are shown in Fig. 10(a) and (b). Fig. 10 shows that many cracks develop on the gauge surface independent of test temperature (550 °C or 600 °C). However, it is hard to distinguish the intergranular cracks from transgranular cracks. According to Was's review [6], all austenitic stainless steels have experienced some degree of SCC, most of which is intergranular. Temperature, oxygen content and strain rate are key parameters that influence the SCC susceptibility. The different research results on the SCC susceptibility of SSs [20–22] may be attributed to the fact that in SSRT tests, apart from temperature, the materials condition, water chemistry and strain rate are all important parameters. So systematical research is needed to reveal the combined interactive effects of different test conditions.

From the gauge section appearance, it can be hard to distinguish intergranular cracks from transgranular cracks. However, the fracture surface clearly distinguishes that intergranular and transgranular cracks (Fig. 10). Many micro-voids also appear on the fracture surface, consistent with a ductile fracture mode. Generally, three methods are recommended to evaluate the SCC susceptibility in high temperature water:

(1) Area percentage of intergranular cracking (IG%) on the fracture surface of the SSRT samples, as used by Tsuchiya [41] and Fujisawa [42];
(2) Crack density and depth on the gauge surface of the SSRT samples, as used by Was [43]. These two methods are very effective for evaluating the SCC susceptibility when there is extensive crack growth. However, when the fracture surface is not regular, or the growth and distribution of the cracks on the gauge surface is not uniform and homogenous, the SCC susceptibility cannot be identified accurately by either method.

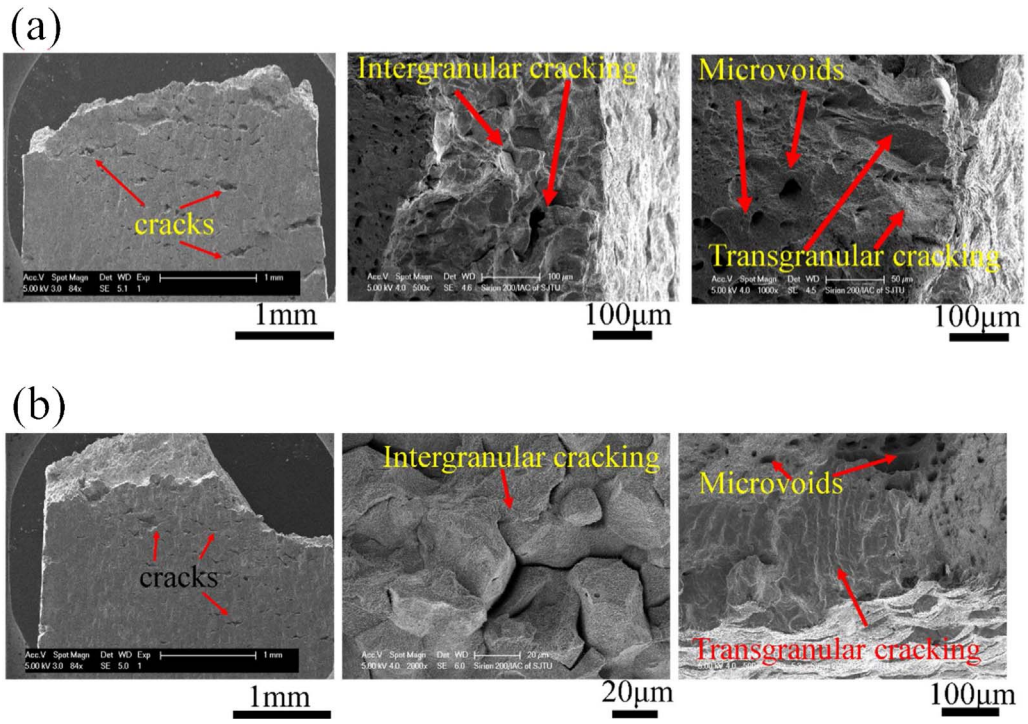

Fig. 10. Gauge section and fracture surface of 316L SS tested in (a) 550 ˚C and (b)600 ˚C SCW.

(3) ASTM also recommends an equation to measure the SCC susceptibility:

$$I_\delta = 1 - \frac{E_u}{E_u(Ar)} \tag{6}$$

where I_δ is the SCC susceptibility index, E_u and $E_u(Ar)$ is the uniform elongation of the materials in water and argon environment, respectively.

Compared with the first two methods, the third method is very simple if the strain to failure in argon at the same temperature is obtained. In the present research, the fracture and gauge surface analysis indicates that SCC susceptibility exists for the 316L SS tested in 550 ˚C and 600 ˚C water, and according to the ASTM standard and Fig. 9, the SCC susceptibility index in 550 ˚C and 600 ˚C SCW is 13.6% and 37.4%, respectively.

The microstructure of the gauge surface of the samples tested in 550 ˚C and 600 ˚C SCW was also examined (Fig. 11). In the observed area, no intergranular or transgranular cracks were observed, as shown in Fig. 11(b), (c) (d) and (e). The EDS mapping analysis indicates that two distinct oxide layers are formed on the SSRT samples: a continuous outer layer that is composed of Fe and O, and an inner layer that is rich in Fe, O and Cr. The outer and inner layers are proved to be Fe_3O_4 and Fe-Cr spinel respectively as discussed in Section 3.1. In the inner layer, areas like 'channels' that are rich in Fe and O, while depleted in Cr, are observed. The 'channels' are distributing both on the original austenitic grain boundaries as well as on the original austenitic grains. This

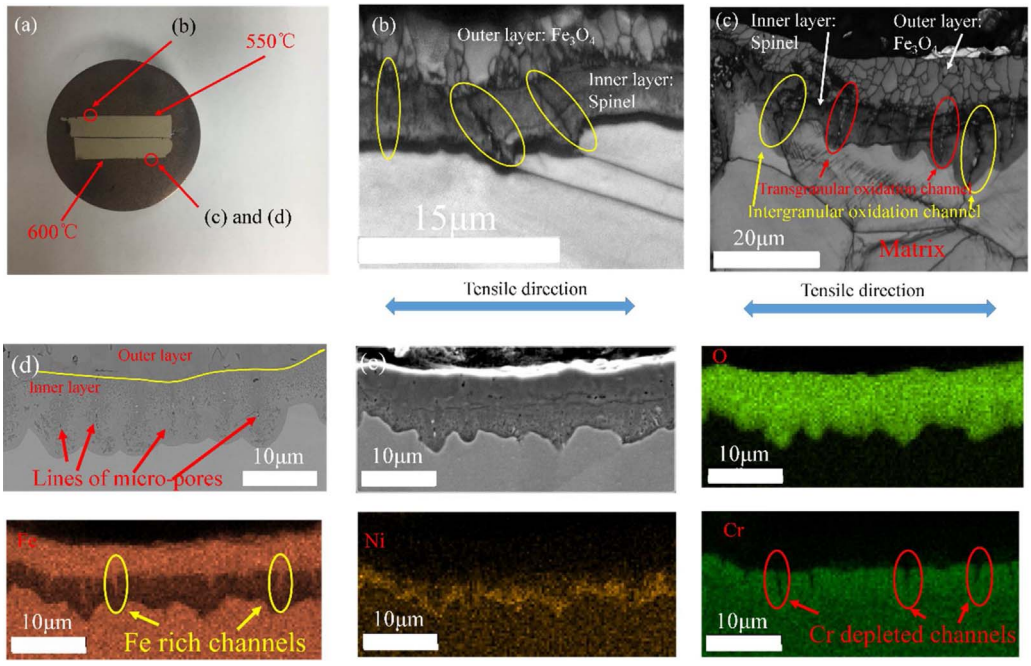

Fig. 11. (a) Image of the tensile specimens, (b) EBSD band contrast of specimen tested in 550 ˚C SCW, (C) EBSD band contrast of specimen tested in 600 ˚C SCW, (d) BSE image of specimen teste at 600 ˚C, (e)SEM and EDS image of the specimen tested in 600 ˚C SCW.

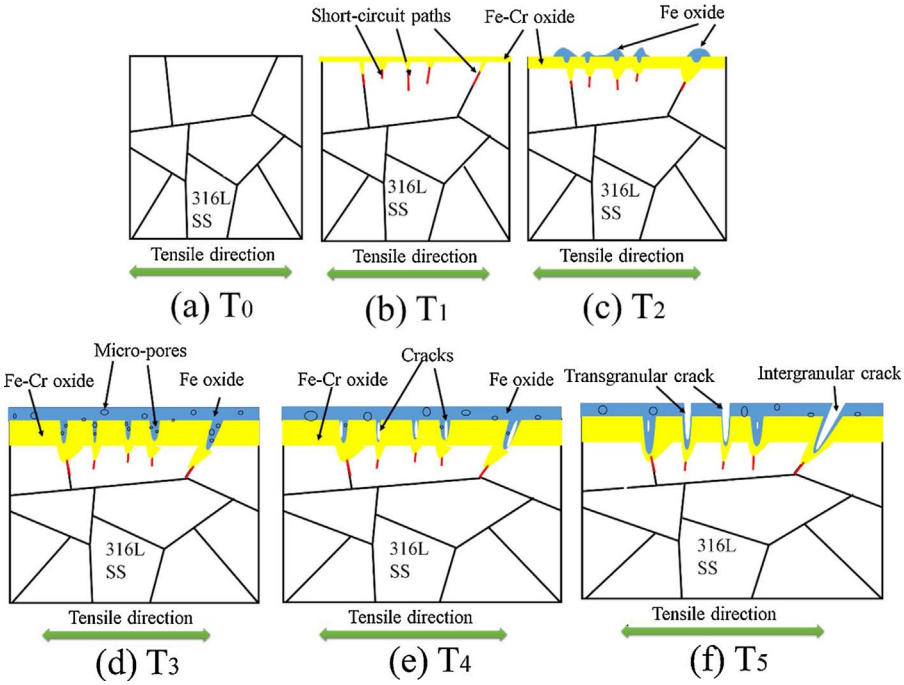

Fig. 12. Schematic showing the process for the formation of cracks on the gauge section of the tensile sample.

phenomenon is greatly different from the results in the general corrosion tests in SCW [44,45]. Fig. 11(d) shows that lines of micro-pores perpendicular to the tensile direction are distributing on the Fe_3O_4 'channels'.

During testing, the materials are subjected to tensile stresses and strains, and the plastic deformation results in the formation of slip offsets. Slip planes, as well as grain boundaries, can act as short-circuit growth path for inward diffusion oxygen or SCW, as schematically shown in Fig. 12(b). The inward diffusion of oxidizing agents leads to oxidation reactions represented by Eqs. (2) and (4), and a Fe-Cr spinel oxide is formed. The oxidation extends into the interior of the material along the short-circuit paths due to the faster diffusion rate of the oxidizing agent (Fig. 12b). Oxidized Fe cations also diffuse outward in this process and the inward diffused oxygen or water can react with the Fe cations to form Fe-oxide along the short circuit paths (Fig. 12c). With increasing test time, the oxide grows (the Fe-Cr oxide layer grows thicker and the Fe-oxide extends deeper into the material) and Fe oxide channels passing through the Fe-Cr oxide film are formed.

The discussion in Section 3.1 indicates that micro-pores can be formed on the Fe-oxide layer, as clearly observed in Fig. 4. For the SSRT specimens, micro-pores are also observed on the Fe oxide channels (Fig. 11d). With increasing test time, lines of pores distributed on the Fe-oxide channels are formed (Fig. 12 d). Since the specimens are subjected to continuous tensile strain and stress, cracks are easily initiated near micro-pores and the subsequent propagation of the cracks results in the connection of the micro-pores (Fig. 12e). The interface between the different phases is always weak, so cracks are also easily formed on the interface when tensile strain is applied to the samples, especially cracks perpendicular to the tensile direction. Compared to the matrix, the Fe_3O_4 oxide layer is fragile, so cracks can propagate to the outer layer of the oxide scale easily, then cracks extending through the entire oxide scale develop (Fig. 12f). The forming of cracks on the Fe_3O_4 channels also leads to faster diffusion of SCW to the Fe-Cr spinel layer, so Fe_3O_4 is also more easily formed in this area. Some of the cracks are repaired by further oxidation and the cracks become smaller (Fig. 12f).

The oxidation kinetics of 600 °C SCW are much higher than at 550 °C, so the Fe_3O_4 'channels' are more easily formed on the SSRT samples tested in 600 °C SCW. This contributes to the more extensive intergranular and transgranular SCC that occurs on the samples tested in 600 °C SCW

4. Conclusions

The corrosion and SCC susceptibility of 316L SS exposed to 550 °C and 600 °C SCW have been investigated, and the results can be summarized as following:

(1) With increasing test temperature, the corrosion rate is greatly increased. A dual layer structure with an outer layer of Fe_3O_4 and an inner layer of $FeCr_2O_4$ is formed. Because of the porous structure of the oxide scale and the absence of a continuous Cr_2O_3 layer, the corrosion rate is high. Fe_2O_3 is not formed in the corrosion process, which can be attributed to two main reasons: (a) the low oxygen content in supercritical water and (b) no compact Cr_2O_3 layer is formed, so Fe cations can diffuse outward continuously to form Fe_3O_4.

(2) Intergranular and transgranular SCC is observed on the SSRT samples tested in 550 °C and 600 °C SCW, with a higher SCC susceptibility at 600 °C. 'Channels' filled with Fe_3O_4 are found on the Fe-Cr spinel layer of the oxide scale, which are formed because water transport paths are formed by tensile straining. The formation of Fe_3O_4 'channels' gives a possible explanation to the intergranular and transgranular SCC that initiates on the surface.

Acknowledgments

This work is financially supported by "National Basic Research Program of China" (No. 2007CB209800). The authors express special thanks to University of Science and Technology Beijing for material preparation.

References

[1] M. Yetisir, Development and integration of Canadian SCWR concept with counter-flow fuel assembly, 6th International Symposium on Supercritical Water-Cooled Reactors (ISSCWR-6), March 3–7, Shenzhen, Guangdong, China, Paper ISSCWR6-13059, 2013.

[2] K.H. Chang, S.M. Chen, T.K. Yeh, J.J. Kai, Effect of dissolved oxygen content on the oxide structure of Alloy 625 in supercritical water environments at 700 °C, Corros.Sci 81 (2014) 21–26.

[3] D.A. Guzonas, W.G. Cook, Cycle chemistry and its effect on materials in a supercritical water-cooled reactor: a synthesis of current understanding, Corros. Sci. 65 (2012) 48–66.

[4] Mizanur Rahman Mohammad, Dongxu Ji, Shahmohammadi Beni Mehrdad, Choi Hei Ho, He Weidong, Zhoa Jiyun, Supercritical water heat transfer for nuclear reactor applications: a review, Ann. Nuc Energy 97 (2016) 53–65.

[5] T. Schulenberga, J. Starflinger, P. Marsault, D. Bittermann, C. Maráczy, E. Laurien, J.A. Lycklama, à nijeholt, H. anglart M. andreani, M., ruzickova, A. toivonen. european supercritical water cooled reactor, Nucl. Eng. Des. 241 (2011) 3505–3513.

[6] G.S. Was, P. Ampornrat, G. Gupta, S. Teysseyre, E.A. West, T.R. Allen, K. Sridharan, L. Tan, Y. Chen, X. Ren, C. Pister, Corrosion and stress corrosion cracking in supercritical water, J. Nucl. Mater. 371 (2007) 176–201.

[7] Lefu Zhang, Kai Chen, Donghai Du, Wenhua Gao, Peter L. Andresen, Xianglong Guo Characterizing the effect of creep on stress corrosion cracking of cold worked Alloy 690 in supercritical water environment, J. Nucl. Mater. 492 (2017) 32–40.

[8] D. Gómez-Briceño, F. Blázquez, A. Sáez-Maderuelo, Oxidation of austenitic and ferritic/martensitic alloys in supercritical water, J. Supercrit. Fluids 78 (2013) 103–113.

[9] Donghui Wen, Beibei Jiang, Qing Wanga, Fengyun Yu, Xiaona Li, Rui Tang, Ruiqian Zhang, Guoqing Chen, Chuang Dong Influences of Mo/Zr minor-alloying on the phase precipitation behavior in modified 310S austenitic stainless steels at high temperatures, Mater. Des. 128 (2017) 34–46.

[10] Xiangyu Zhong, Xinqiang Wu, En-Hou Han, Characteristics of oxidation and oxygen penetration of alloy 690 in 600 °C aerated supercritical water, J. Mater. Sci. Tech. (2017) (in press).

[11] Xiangyu Zhong, En-Hou Han, Xinqiang Wu, Corrosion behavior of Alloy 690 in aerated supercritical water, Corros.Sci 66 (2013) 369–379.

[12] R. Novotný, P. Janík, S. Penttilä, P. Hähner, J. Macákc, J. Siegl, P. Hau, šild, High Cr ODS steels performance under supercritical water environment, J. Supercrit. Fluids 81 (2013) 147–156.

[13] J. Isselin, R. Kasada, A. Kimura, Corrosion behaviour of 16%Cr?4%Al and 16%Cr ODS ferritic steels under different metallurgical conditions in a supercritical water environment, Corros Sci. 52 (2010) 3266–3270.

[14] Seong Sik Hwang, Byung Hak Lee, Jung Gu Kim, Jinsung Jang, SCC and corrosion evaluations of the F/M steels for a supercritical water reactor, J. Nucl Mater. 372 (2008) 177–181.

[15] H.S. Cho, A. Kimura, S. Ukai, M. Fujiwara, Corrosion properties of oxide dispersion strengthened steels in super-critical water environment, J. Nucl. Mater. 329-333 (2004) 387–391.

[16] Xingying Tang, Shuzhong Wang, Lili Qian, Yanhui Li, Zonghu Lin, Donghai Xu, Yupeng zhang, Corrosion behavior of nickel base alloys, stainless steel and titanium alloy in supercritical water containing chloride, phosphate and oxygen, Chem. Eng. Res. Des. 100 (2015) 530–541.

[17] Zhao Shen, Lefu Zhang, Rui Tang, Qiang Zhang, The effect of temperature on the SSRT behavior of austenitic stainless steels in SCW, J. Nucl. Mater. 454 (2014) 274–282.

[18] Yashar Behnamian, Amir Mostafaeib, Alireza Kohandehghan, Babak shalchi amirkhiz, dominic serate, yifei sun, subiao liu, ermia aghaie, yimin zeng, markus chmielus, wenyue zheng, david guzonasd, weixing chen, jing Li luo, a comparative study of oxide scales grown on stainless steel and nickel-based superalloys in ultra-high temperature supercritical water at 800 °C, Corros.Sci 106 (2016) 188–207.

[19] Edouard Asselin, Akram Alfantazi, Steven Rogak, Corrosion of nickel-chromium alloys, stainless steel and niobium at supercritical water oxidation conditions, Corros.Sci. 52 (2010) 118–124.

[20] A. Sáez-Maderuelo, D. Gómez-Briceño, Stress corrosion cracking behavior of annealed and cold worked 316L stainless steel in supercritical water, Nucl. Eng. Des. 307 (2016) 30–38.

[21] S. Teysseyre, G.S. Was, Stress corrosion cracking of austenitic alloys in supercritical water, Corrosion 62 (2006) 1100–1116.

[22] Zhao Shen, Lefu Zhang, Rui Tang, Qiang Zhang, SCC susceptibility of type 316Ti stainless steel in supercritical water, J. Nucl. Mater. 458 (2015) 206–215.

[23] Y. Chen, K. Sridharan, S. Ukai, T.r. Allen, Corrosion of 9Cr oxide dispersion strengthened steel in supercritical water environment, J. Nucl. Mater. 371 (2007) 118–128.

[24] G.S. Was, S. Teysseyre, Z. Jiao, Corrosion of austenitic alloys in supercritical water, Corrosion 62 (2006) 989–1005.

[25] Yashar Behnamian, Amir Mostafaei, Alireza Kohandehghan, Babak Shalchi Amirkhiz, Ramin Zahiri, Wenyue Zheng, David Guzonas, Markus Chmielus, Weixing Chen, Jing Li Luo, A comparative study on the oxidation of austenitic alloys 304 and304-oxide dispersion strengthened steel in supercritical water at 650 °C, J. Supercrit. Fluids 119 (2017) 245–260.

[26] Naiqiang Zhang, Zhongliang Zhu, Guoqiang Yue, Dongfang Jiang, Hong Xu, The oxidation behaviour of an austenitic steel in deaerated supercritical water at 600–700°C, Mater. Charact. 132 (2017) 119–125.

[27] Kashif I. Choudhry, Shooka Mahboubi, Gianluigi A. Botton, Joseph R. Kish, Igor M. Svishchev, Corrosion of engineering materials in a supercritical water cooled reactor: characterization of oxide scales on Alloy 800H and stainless steel 316, Corros. Sci. 100 (2015) 222–230.

[28] I.G. Wright, R.B. Dooley, A review of the oxidation behavior of structural alloys in steam, Int. Mater. Rev. 55 (2010) 129–167.

[29] Yashar Behnamian, Amir Mostafaei, Alireza Kohandehghan, Babak shalchi amirkhiz, daniel serate, wenyue zheng, david guzonas, markus chmielus, weixing chen, JingLiLuo, characterization of oxide scales grown on alloy 310S stainless steel after long term exposure to supercritical water at 500 °C, Mater. Charact. 120 (2016) 273–328.

[30] L. Tan, Y. Yang, T.R. Allen, Oxidation behavior of iron-based alloy HCM12A exposed in supercritical water, Corros. Sci. 48 (2006) 3123–3138.

[31] Y. Behnamian, A. Mostafaei, A. Kohandehghan, B.S. Amirkhiz, D. Serate, Y. Sun, S. Liu, E. Aghaie, Y. Zeng, M. Chmielus, W. Zheng, D. Guzonas, W. Chen, J.-L. Luo, A comparative study on corrosion behavior of stainless steel and nickel-based superalloys in ultra-high temperature supercritical water at 800 °C, Corros. Sci. 106 (2016) 188–207.

[32] Y. Chen, K. Sridharan, T. Allen, Corrosion behavior of ferritic-martensitic steel T91 in supercritical water, Corros. Sci. 48 (2006) 2843–2854.

[33] J. Bischoff, A.T. Motta, C. Eichfeld, R.J. Comstock, G. Cao, T.R. Allen, Corrosion of ferritic–martensitic steels in steam and supercritical water, J. Nucl Mater. 441 (2013) 604–611.

[34] Lizhen Tan, Ying Yang, Todd R. Allen, Porosity prediction in supercritical water exposed ferritic/martensitic steel HCM12A, Corros. Sci. 48 (2006) 4234–4242.

[35] Xiangyu Zhong, Xinqiang Wu, En-Han Han, Effects of exposure temperature and time on corrosion behavior of a ferritic–martensitic steel P92 in aerated supercritical water, Corros. Sci. 90 (2015) 511–521.

[36] J. Zurek, E. De Bruycker, S. Huysmans, W.J. Quadakkers, Steam oxidation of 9–12%Cr steels: critical evaluation and implications for practical application, Corrosion 70 (2014) 112–129.

[37] Vasisht Venkatesh, H.J. Rack, Elevated temperature hardening of INCONEL 690, Mech. Mater. 30 (1998) 69–81.

[38] T.S. Byun, On the stress dependence of partial dislocation separation and deformation microstructure in austenitic stainless steels, Acta Mater. 51 (2003) 3063–3071.

[39] J. Talonen, H. Hänninen, Formation of shear bands and strain-induced martensite during plastic deformation of metastable austenitic stainless steels, Acta Mater. 55 (2007) 6108–6118.

[40] R. Novotny, P. Hähner, J. Siegl, P. Haušild, S. Ripplinger, S. Penttilä, A. Toivonen, Stress corrosion cracking susceptibility of austenitic stainless steels in supercritical water conditions, J. Nucl. Mater. 409 (2011) 117–123.

[41] Y. Tsuchiya, F. Kano, N. Saito, A. Shioiri, S. Kasahara, K. Moriya, H. Takahashi, GENES4/ANP2003 Kyoto Japan, (2003) (Paper 1096).

[42] R. Fujisawa, K. Nishimura, T. Kishida, M. Sakaihara, Y. Kurata, Y. Watanabe, Corrosion, NACE International, Houston, Texas, USA, 2005 (paper 05395).

[43] G.S. Was, S. Teysseyre, Proceeding of 12th International Conference on Environmental Degradation of Materials in Nuclear Power Systems-Water Reactors, The Minerals, Materials and Metals Society, Warrendale, PA, USA, 2005 (Paper 1343).

[44] Stéphane Sarrade, Damien Féron, Fabien Rouillard, Stéphane Perrin, Raphael Robin, Jean-Christophe Ruiz, Hubert-Alexandre Tur, Overview on corrosion in supercritical fluids, J. Supercrit. Fluids 120 (2) (2017) 335–344.

[45] D. Guzonas1, R. Novotny, S. Penttilä, Corrosion phenomena induced by supercritical water in Generation IV nuclear reactors Structural Materials for Generation IV Nuclear Reactors, (2017), pp. 105–152.